A Frequency Domain Model for Generating B-Mode Images with Array Transducers

Yadong Li and James A. Zagzebski, *Associate, IEEE*

Abstract—**A frequency domain B-mode imaging model applicable to linear and phased array transducers was developed for simulating ultrasound images of random media. Computations are based on an approximation that is less restrictive than the Fresnel approximation. The model is compared with the exact time domain impulse response method, regarded as the "gold standard". In a typical application, errors in simulated rf waveforms are less than 1% regardless of the steering angle for distances greater than 2 cm, yet computation times are on the order of $\frac{1}{150}$ of those using the exact method. This model takes into account the effects of frequency-dependent attenuation, backscattering, and dispersion. Modern beam-forming techniques such as apodization, dynamic aperture, elevational focusing, multiple transmit focusing, and dynamic receiving focusing also can be simulated.**

I. Introduction

LINEAR and curved linear array transducers generally are used in modern medical ultrasound imaging. They can be steered and focused during transmission and reception. To optimize image quality, many different designs and imaging techniques have been studied and applied. Accurate and efficient simulation models assist researchers in analyzing and improving the spatial resolution, image contrast, and other aspects of image quality for these devices.

A number of transducer field simulation methods and B-mode image models have been described in the literature. They roughly fall into two categories: frequency-domain models and time-domain models. Frequency-domain simulation techniques are based on diffraction theory for continuous waves. Various approximations can be made to reduce the computational complexity, and these lead to different degrees of accuracy and efficiency. Time-domain simulations are based on the impulse response of a radiator at the chosen field points [1], [2]. Closed form expressions for the impulse response function have been derived for many geometries [3], [4]. The impulse response generally exhibits discontinuities, which leads to the need for very high temporal sampling rates to obtain accurate results for the field. However, the closed-form time domain solution is exact for all field locations. Therefore, other methods can be evaluated in terms of accuracy and efficiency by comparing with the closed-form impulse response method.

Crombie *et al.* [6] studied the accuracy and efficiency of several beam simulation schemes. They concluded that, in the frequency domain, the Fresnel approximation [7] yields the most accurate results for an unsteered array; however, the accuracy degrades with increasing steering angle. They also showed that the Fresnel approximation is generally more efficient than the exact time domain method.

Jensen and Svendsen [8] and Jensen and Munk [9] have demonstrated that realistic B-mode images can be generated by using the time-domain impulse response method to calculate the transducer field, even when approximations are used to reduce the computational complexity. Turnbull and Foster [10] did an extensive study of 2-D arrays using the time-domain method. Lu and Greenleaf [11] applied a frequency-domain model in their simulations of beams and images generated by "limited diffraction" transducers.

We have developed a frequency-domain B-mode imaging model for rectangular-element array transducers that is based on a less restrictive approximation than the Fresnel approximation. In this report, we show that the model yields accurate simulations even when the beam is steered at large angles. This model is very flexible as it readily incorporates frequency-dependent attenuation, backscattering, and dispersion. Imaging techniques, such as dynamic focusing, dynamic aperture, and apodization, also have been built in.

II. Theory

In a homogeneous medium, if a rectangular transducer surface of width a and length b is embedded in an infinite rigid baffle, and is vibrating at an angular frequency ω (i.e., the velocity of the surface is $v(t) = u(\omega)e^{-i\omega t}$), the pressure field can be written as [13]:

$$p_i(\vec{r}, \omega) = -\frac{i\rho k c u(\omega)}{4\pi} A_0(\vec{r}, \omega) \qquad (1)$$

where

$$A_0(\vec{r}, \omega) = \int\limits_{-\frac{b}{2}}^{+\frac{b}{2}} \int\limits_{-\frac{a}{2}}^{+\frac{a}{2}} \frac{e^{ik|\vec{r}-\vec{r'}|}}{|\vec{r}-\vec{r'}|} \, dx'dy'. \qquad (2)$$

Here ρ is the density of the medium, c is the speed of sound, $k = \frac{\omega}{c}$ is the wave number, $\vec{r}$ is the field point, and $\vec{r'}$ is a source point on the surface of the transducer. The coordinate system is shown in Fig. 1. If the medium is dispersive, $c(\omega)$ can be used in place of c. Attenuation
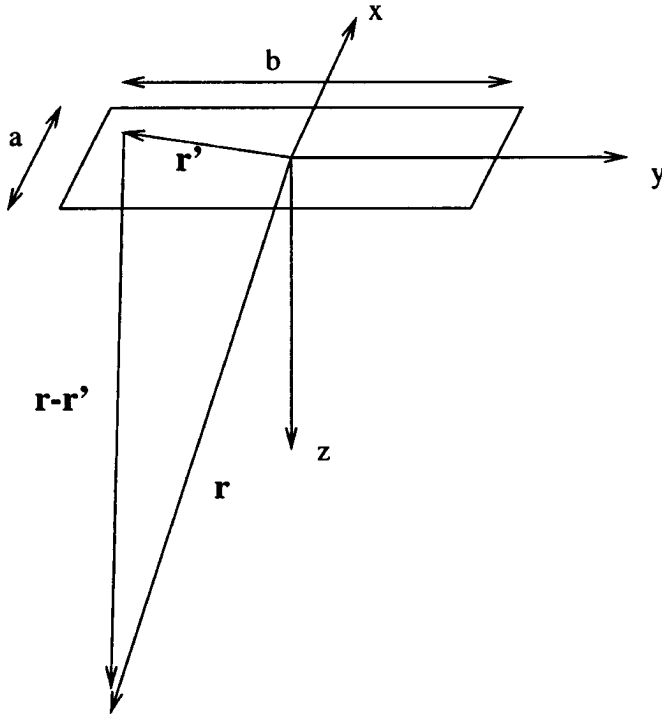
Fig. 1. Coordinate system used for computing the field from a rectangular element.

is taken into account by replacing k by a complex wave number $K = \frac{\omega}{c(\omega)} + i\alpha(\omega)$, where $\alpha(\omega)$ is the attenuation coefficient.

The task in any model for the beam from a transducer is to compute the integral, such as (2), as efficiently as possible.

A. Approximation Scheme

For typical linear and phased arrays, usually the length of the transducer element b is on the order of 1 cm and the width is on the order of half a wavelength, resulting in the condition $b \gg a$. Define r to be the distance from the field point to the center of the element. Under the assumption that $r > b \gg a$, $|\vec{r} - \vec{r'}|$ can be expanded by:

$$|\vec{r} - \vec{r'}| = \sqrt{(x - x')^2 + (y - y')^2 + z^2}$$
$$\approx r + \frac{1}{2r}(x'^2 + y'^2 - 2xx' - 2yy') \qquad (3)$$
$$- \frac{1}{8r^3}(x'^2 + y'^2 - 2xx' - 2yy')^2$$

where x, y, and z are the coordinates of the field point. We can take advantage of the fact that, if $a \approx \frac{\lambda}{2}$, terms on the order of $\frac{x'^2}{2r}$ are negligible for the y' integration in (2). This will introduce a phase error of $\frac{kx'^2}{2r} < \frac{ka^2}{8r} \approx \frac{\pi\lambda}{16r}$ at most, which is smaller than 0.007 radians in the case when r is greater than 1 cm and the wavelength is around 300 μm (1500 ms^{-1}/5 MHz).

Therefore,

$$|\vec{r} - \vec{r'}| \approx r + \frac{1}{2r}(y'^2 - 2xx' - 2yy')$$
$$- \frac{1}{8r^3}(x'^2 + y'^2 - 2xx' - 2yy')^2. \quad (4)$$

In the region where $\frac{k}{8r^3}(x'^2 + y'^2 - 2xx' - 2yy')^2 \ll 1$ radian, $|\vec{r} - \vec{r'}|$ can be approximated using the first two terms. This approximation is less restrictive than the Fresnel approximation, which is written as [7]:

$$|\vec{r} - \vec{r'}| = \sqrt{(x - x')^2 + (y - y')^2 + z^2}$$
$$\approx z + \frac{1}{2z}[(x - x')^2 + (y - y')^2] \qquad (5)$$
$$- \frac{1}{8z^3}[(x - x')^2 + (y - y')^2]^2.$$

The Fresnel approximation requires $\frac{k}{8z^3}[(x - x')^2 + (y - y')^2]^2 \ll 1$ radian for reasonable accuracy. The error using the Fresnel approximation is on the order of $O\left(\frac{x^4 + y^4}{z^3}\right)$, while the error using the approximation in (4) is on the order of $O\left(\frac{x^2 + y^2}{r^3}\right)$. When the beam is steered at a large angle (i.e., x is comparable to z), the Fresnel approximation will not hold; however, (4) is still valid as long as r is not too small, i.e., $\frac{k}{8r^3}(x'^2 + y'^2 - 2xx' - 2yy') < 1$.

Keeping only the first two terms in (4): $|\vec{r} - \vec{r'}| \approx r + \frac{1}{2r}(y'^2 - 2xx' - 2yy')$, and

$$A_0(\vec{r}, \omega) \approx \frac{a}{r}e^{ikr} \operatorname{sinc}\left(\frac{kxa}{2\pi r}\right) \int_{-\frac{b}{2}}^{\frac{b}{2}} e^{ik\frac{y'^2 - 2yy'}{2r}} \, dy'. \qquad (6)$$

The 2-D integral in (2) is reduced to a 1-D integral. The remaining integral has to be done numerically. Note that the sinc function is a result of ignoring the term $\frac{x'^2}{2r}$. If $\frac{x'^2}{2r}$ cannot be ignored (i.e., the width of the array element is much larger than λ), the integration in the x' direction also must be done numerically.

B. Elevational Focusing

A fixed elevational focus is applied using a mechanical lens in most linear and phased array transducers. To simulate focusing the element elevationally at a distance F_e, a phase factor of $e^{-i\omega t_e(F_e, y')}$ is added into (6), where $t_e(F_e, y') = \frac{1}{c}\left(\sqrt{y'^2 + F_e^2} - F_e\right) \approx \frac{y'^2}{2cF_e}$. The approximation is made by using the fact that, usually the elevational focus is much longer than the half-length of the element, i.e., $|y'| < \frac{b}{2} \ll F_e$. In the usual case in which $b = 1$ cm, $F_e = 5$ cm, $c = 1540$ m/s and 5 MHz frequency, the phase error caused by this approximation is only 0.013 radian. Therefore,

$$A_0(\vec{r}, \omega) = \frac{a}{r}e^{ikr} \operatorname{sinc}\left(\frac{kxa}{2\pi r}\right) \int_{-\frac{b}{2}}^{\frac{b}{2}} e^{ik\left(\frac{y'^2 - 2yy'}{2r} - \frac{y'^2}{2F_e}\right)} \, dy'. \qquad (7)$$

Equation (7) can be rewritten in a form that is more convenient for numerical evaluation:

$$A_0(\vec{r}, \omega) =$$

$$\begin{cases} \frac{a}{r}\sqrt{\frac{\pi}{2k\beta}} e^{ikr} \operatorname{sinc}\left(\frac{kxa}{2\pi r}\right) e^{-ik\frac{y^2}{4r^2\beta}} \int_{t_1}^{t_2} e^{i\frac{\pi}{2}t^2}\, dt & (\beta > 0) \\ \frac{ab}{r} e^{ikr} \operatorname{sinc}\left(\frac{kxa}{2\pi r}\right) \operatorname{sinc}\left(\frac{kyb}{2\pi r}\right) & (\beta = 0) \\ \frac{a}{r}\sqrt{-\frac{\pi}{2k\beta}} e^{ikr} \operatorname{sinc}\left(\frac{kxa}{2\pi r}\right) e^{-ik\frac{y^2}{4r^2\beta}} \int_{t_1}^{t_2} e^{-i\frac{\pi}{2}t^2}\, dt & (\beta < 0) \end{cases} \quad (8)$$

where $\beta = \frac{1}{2r} - \frac{1}{2F_e}$, $t_1 = \sqrt{\frac{2k|\beta|}{\pi}}\left(-\frac{b}{2} - \frac{y}{2r\beta}\right)$ and $t_2 = \sqrt{\frac{2k|\beta|}{\pi}}\left(\frac{b}{2} - \frac{y}{2r\beta}\right)$.

The term $\int_{t_1}^{t_2} e^{\pm i\frac{\pi}{2}t^2}\, dt$ is called the Fresnel integral, which can be evaluated very efficiently by a numerical method [12]. Equation (8) incorporates elevational focusing into the model without adding significant computational cost.

C. Lateral Array Steering and Focusing

For a linear or phased array shown in Fig. 2, the integral in (2) over N active elements is:

$$A(\vec{r}, \omega) = \sum_{n=1}^{N} a(n) A_{0n}(\vec{r}, \omega) e^{-i\omega t(n, F_x, F_z)} \quad (9)$$

where $a(n)$ is an apodization factor for the nth element. The parameter $t(n, F_x, F_z)$ is the time delay needed to steer and focus the beam to (F_x, F_z) in the image $(x-z)$ plane; $t(n, F_x, F_z) = \frac{1}{c}\Big(\sqrt{[(n - \frac{1+N}{2})d - F_x]^2 + F_z^2} - \sqrt{F_x^2 + F_y^2}\Big)$; and d is the center-to-center distance between elements.

D. Pulse-Echo Imaging

Clinical scanners operate in a pulse-echo mode. Under the assumption of local plane waves and the Born approximation, the scattered wave from a single scatterer at $\vec{r}$ is [13], [14]:

$$p_s(\vec{r''}, \omega) = p_i(\vec{r}, \omega)\frac{e^{ik|\vec{r} - \vec{r''}|}}{|\vec{r} - \vec{r''}|}\Phi(\omega, \theta) \quad (10)$$

where $\vec{r''}$ is the field point of the scattered wave; $\vec{r}$ is the location of the scatterer; $p_i(\vec{r}, \omega)$ is the incident wave at the scatterer location; and $\Phi(\omega, \theta)$ is called the angular distribution factor, which quantifies the scattered amplitude in the direction of azimuth angle θ [13].

When the sizes of the scatterers are much smaller than the incident wavelength, i.e., $ka \ll 1$, Φ is reduced to Rayleigh scattering [13]:

$$\Phi(\omega, \theta) = \frac{1}{3}k^2 a_s^3\left(\frac{\kappa_e - \kappa}{\kappa} + \frac{3\rho_e - 3\rho}{2\rho_e - \rho}\cos\theta\right) \quad (11)$$
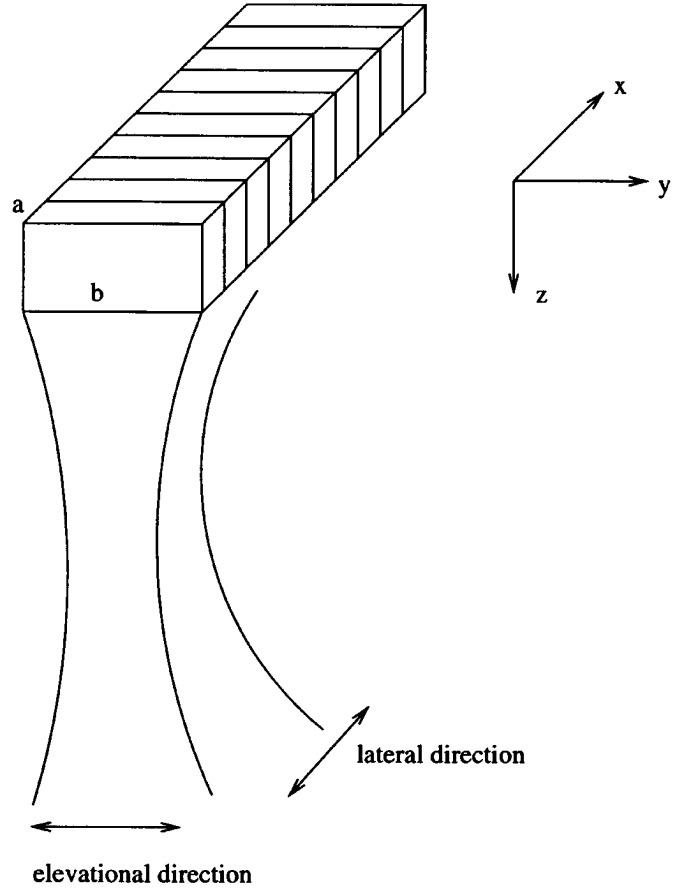

Fig. 2. Array of rectangular elements, each has dimensions $a \times b$, as simulated using the frequency-domain model.

where a_s is the radius of the scatterer; θ is the azimuthal angle; κ_e is the compressibility of the material of the scatterer; κ is the compressibility of the medium; ρ_e is the density of the scatterer; and ρ is the density of the medium. As a first order approximation, it is assumed that the density of the scatterer is approximately equal to that of the surrounding medium. This eliminates the θ dependence and leaves only a monopole term.

The backscattered force from a single scatterer detected by the transducer is the integral of the backscattered pressure over the transducer surface:

$$f(\vec{r}, \omega) = \iint_S p_s(\vec{r''}, \vec{r})\, dx''dy''$$

$$= -\frac{i\rho}{4\pi}kcu(\omega)\Phi(\omega)A^T(\vec{r}, \omega)A^R(\vec{r}, \omega) \quad (12)$$

where the $A^T(\vec{r}, \omega)$ models the transmit profile, and $A^R(\vec{r}, \omega)$ models the receiving profile. Dynamic receive-focus can be achieved by varying the F_x, F_z in the $A^R(\vec{r}, \omega)$ term according to the location of the scatterer. The total force on the array when multiple scatterers are present can

be simulated by superposition:

$$F(\omega) = \sum_{i=1}^{M} f(\vec{r_i}, \omega)$$

$$= -\frac{i\rho}{4\pi} kcu(\omega) \sum_{i=1}^{M} \Phi_i(\omega) A^T(\vec{r_i}, \omega) A^R(\vec{r_i}, \omega) \quad (13)$$

where M is the total number of scatterers.

The final time-domain signal can be expressed as:

$$V(t) = \int_{0}^{\infty} T(\omega) F(\omega) e^{-i\omega t} \, d\omega \quad (14)$$

where $T(\omega)$ is a coefficient for converting force on the transducer to a voltage. This usually will depend on the frequency.

III. ACCURACY AND EFFICIENCY OF THE METHOD

A. Comparison of Methods

In this section, we compare the accuracy and efficiency of our method with that of previously described models. The models chosen are: the exact time-domain impulse response as described by San Emeterio and Ullate [3] using a temporal sampling rate of 4.096 GHz for the impulse response function; the same algorithm as method 1, but at sampling rates of 1.024 GHz, 512 MHz, 256 MHz, and 128 MHz; a frequency-domain simulation using the Fresnel approximation; and the algorithm described in this paper.

We calculated the pressure field of a 32-element segment of a linear array, with element dimensions of 150 μm $\times$ 10 mm and center-to-center spacings of 200 μm. Furthermore, we assumed a rigid baffle, no apodization, and $c = 1540$ m/s. It was assumed that each element has a surface velocity that is described by a Gaussian function in time (Fig. 3), with a center frequency of 5 MHz, a 3 dB bandwidth of 2.45 MHz, and unit amplitude. The array is laterally focused at a fixed distance of 25 mm, and no elevational focusing is applied. For simplicity, this study only calculated the transmitted field and ignored attenuation and dispersion.

For purposes of the computation, the error of Method 1, with a 4.096 GHz sampling rate in the time domain, was assumed to be negligible because increasing the sampling rate further resulted in little difference in the results. The solution given by method 1 was used as a standard for error evaluation. The performance of the four algorithms was compared for five steering angles (0 to 40°, in 10° steps) and at 10 distances (15 mm to 60 mm, in 5 mm steps). Crombie *et al.* [6], evaluating the same conditions, used the "6-dB resolution" as a measure of accuracy. However, in this work we chose to compare the rf waveforms generated by methods 2, 3, and 4 more directly with those produced by method 1. Thus for each steering angle θ and distance r, rf waveforms were calculated using each of the
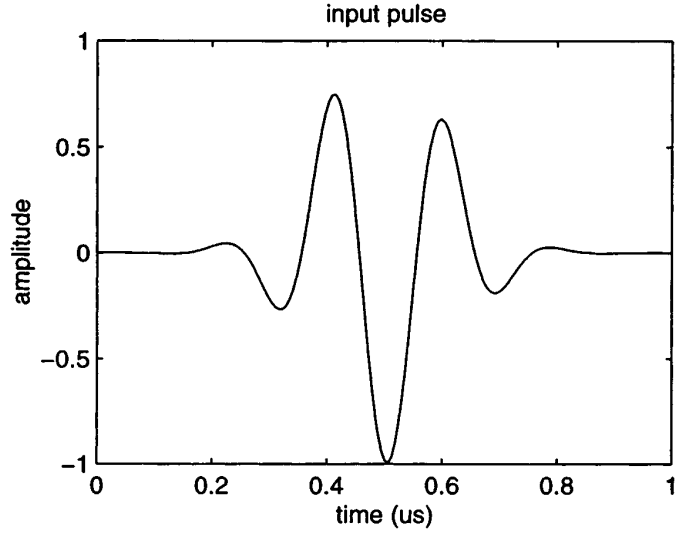

Fig. 3. Assumed velocity waveform of the transducer element surface, used for comparing performance of the frequency domain beam model with time-domain models.

four methods; calculations were done at 21 field points along a line of length 1 cm in the lateral direction of the image plane. These 21 waveforms contain detailed information on how the ultrasound field evolves with time at the location (r, θ) and its vicinity in the imaging plane.

At each (r, θ) location, a normal relative error was calculated using:

$$\text{Error}\% = 100 \times \sqrt{\frac{\sum_{i,j}[V_i(t_j) - V_i^R(t_j)]^2}{\sum_{i,j}[V_i^R(t_j)]^2}} \quad (15)$$

where $V_i(t_j)$ is the value of the ith waveform sampled at time t_j, and $V_i^R(t_j)$ is the waveform computed using the exact solution, i.e., from method 1. In addition, a maximum error for location (r, θ) was computed by applying (15) to each of the 21 waveforms individually and retaining the maximum value at that location. This was done for each method. The normal error measures the overall accuracy of the method around the location (r, θ), and the maximum error is an indicator of the error spread, a larger maximum error implying a wider spread.

Because the time-domain impulse response method uses a much higher sampling rate than the frequency-domain method, a resample of the signal produced by the time-domain solution was performed using the sampling rate of the frequency domain method before the error evaluation. This decimation of the response is done by simply removing samples. The sampling rate of the time-domain method was chosen to be integer multiples of that in the frequency domain, so the resampling process did not introduce errors due to time mismatches.

B. Results

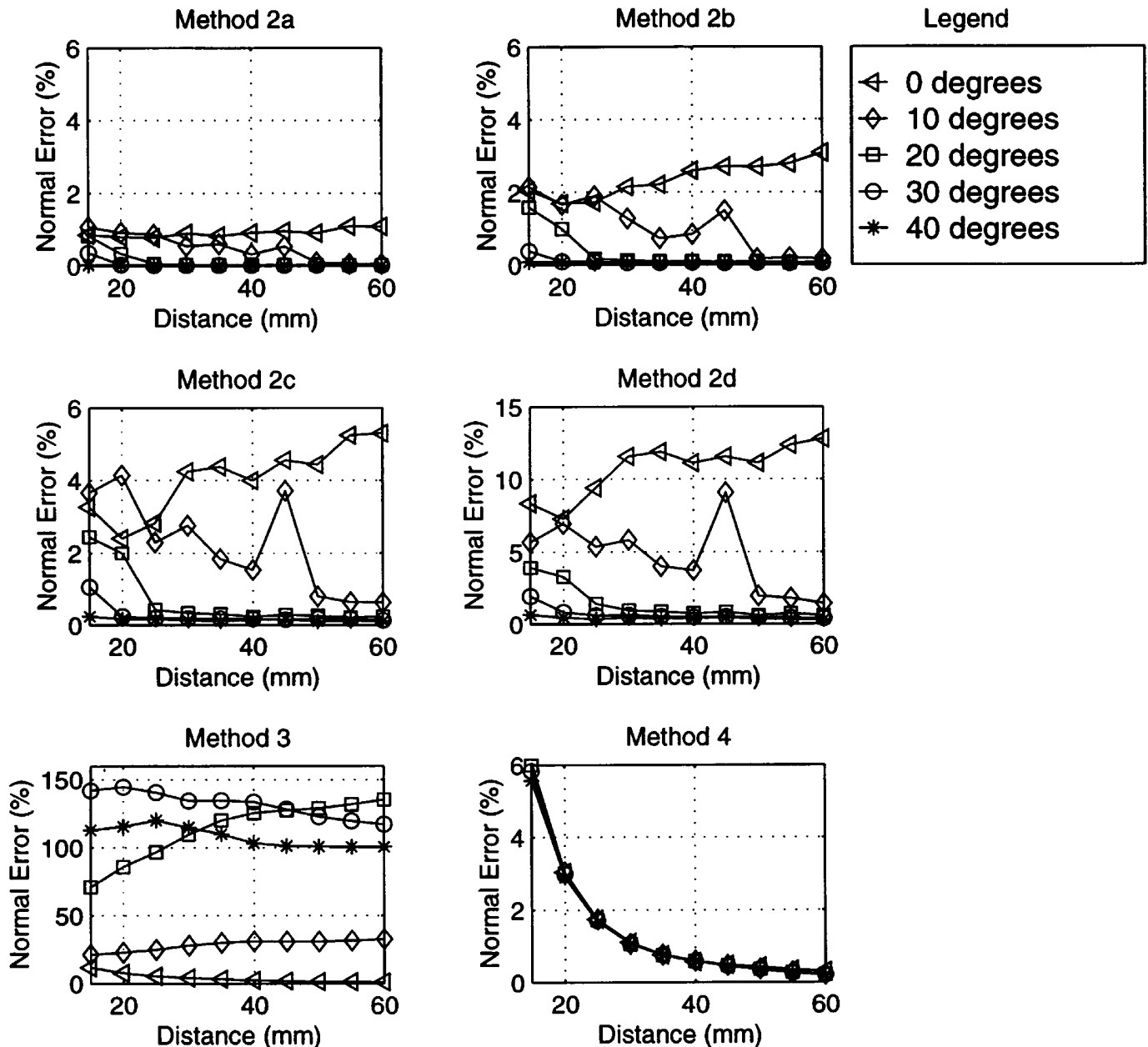Figs. 4 and 5 plot the normal and maximum error of the three approximation methods. Results are shown for

Fig. 4. Comparisons of normal errors at different steering angles for the three relatively efficient beam models (methods 2, 3, and 4). Method 4 is the frequency-domain model described here. The error is calculated by comparing computed waveforms with the rf waveform obtained using method 1. Method 2a, 2b, 2c, and 2d use sampling rates of 1.024 GHz, 512 MHz, 256 MHz, and 128 MHz, respectively.

five steering angles and 10 distances. To show the angle dependence more clearly, Figs. 6 and 7 plot the average error over a 25 mm to 60 mm distance for the different steering angles.

These results show that the errors of methods 2 and 3 depend on the steering angle. Method 2 becomes less accurate when the steering angle is small. This applies to all sampling rates and is caused by the discontinuities of the impulse response function at field points close to the axis of the transducer. For small steering angles (0° to 10°), even a high sampling rate of 1.024 GHz results in a maximum error of 10% in the time domain signal (Fig. 5, top left). However, for large steering angles (> 20°), even a modest

sampling rate, such as 256 MHz, leads to very accurate results (Fig. 4, method 2c). As expected, the accuracy of method 2 improves with a higher sampling rate. Some authors have applied "adaptive" methods to enable use of lower sampling rate at which impulse response function exhibits sharp discontinuities [5].

In contrast, the error of method 3 is small for a 0° steering angle but becomes unacceptable when the steering angle is larger than 20°. This is in agreement with the characteristics of the error term in (5) as well as with the results of Crombie *et al.* [6]. Method 4, however, shows very small normal and maximum errors at all steering angles. The error of method 4 is nearly independent of the steering
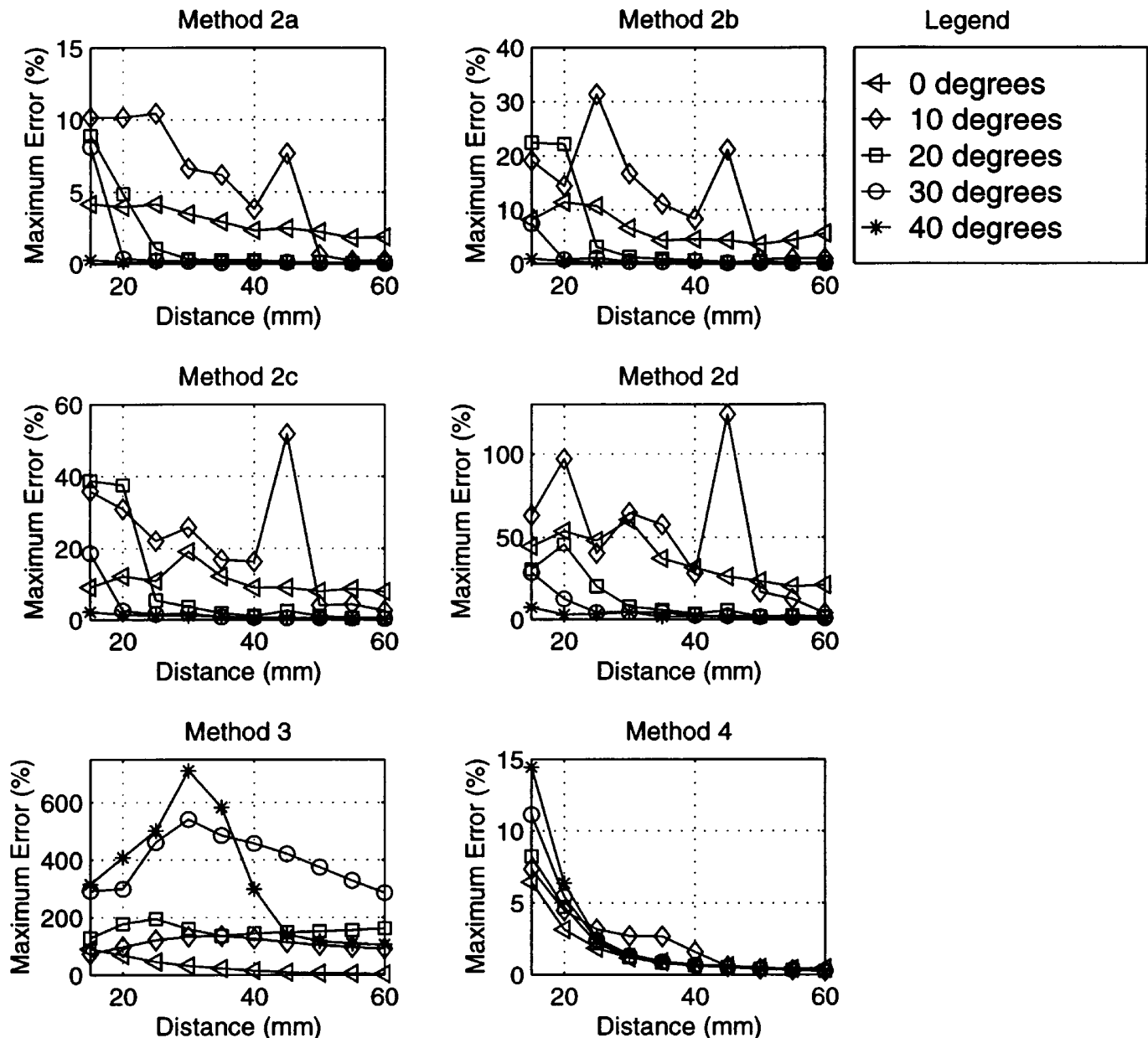
Fig. 5. Comparisons of maximum errors at different steering angles for methods 2, 3, and 4. Method 4 is the frequency domain model described here. Method 2a, 2b, 2c, and 2d use sampling rates of 1.024 GHz, 512 MHz, 256 MHz, and 128 MHz, respectively.

angle, and it decreases with distance. For the condition simulated, when the distance is greater than 20 mm, the maximum error is uniformly smaller than 8% for all steering angles. The bar plots in Fig. 6 and 7 show that at small steering angles, the normal error of method 4 is comparable with that of method 2a, and the maximum error of method 4 is even smaller than that of method 2a. These results demonstrate that the error of method 4 is small and has a very narrow spread.

The efficiency of the different methods is illustrated by comparing their computation time. The computation time was recorded for calculating a waveform of length 32 μs. For the frequency domain method, we choose to use 1024 sampling points at a sampling rate of 32 MHz (1024/32 MHz = 32 μs), which implies that the calcula-

tion has to be done in the frequency domain in 1/32 MHz (32 MHz/1024) increments up to the Nyquist frequency (16 MHz in this case).

Computation times were normalized to the time for method 1, and results are presented in Fig. 8. For the transducer parameters simulated, the frequency-domain method described in this paper is about 155 times faster than the well-sampled time domain method. To match the computation time of the frequency-domain method, the sampling rate of the time-domain method has to be less than 128 MHz (method 2d). However, for this sampling rate, the error is large and varies widely for small steering angles. The machine used for this test contains an Alpha 500 MHz 21164 processor, 1 MB L3 cache and 128 MB memory. The computation time of the time-
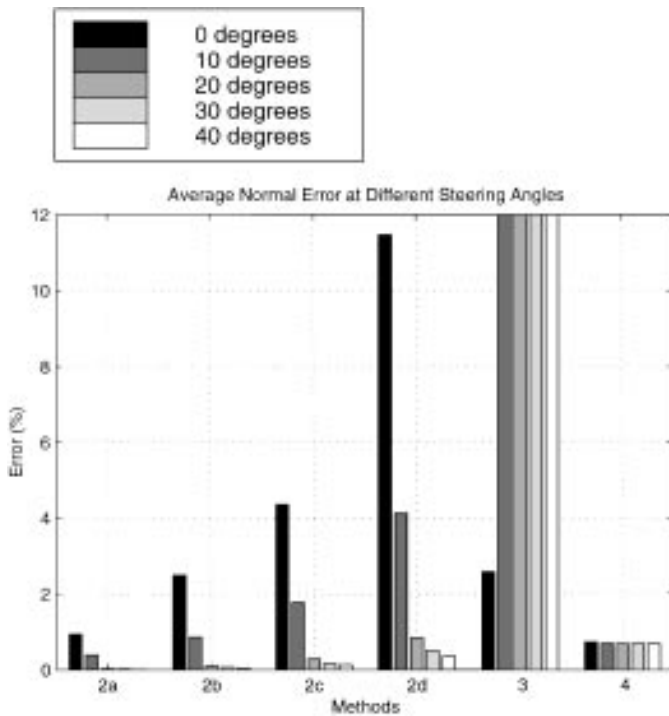
Fig. 6. Bar plots of average normal error at different steering angles for methods 2, 3, and 4. The errors of method 3 at steering angles larger than 10° are outside the range of the plot.
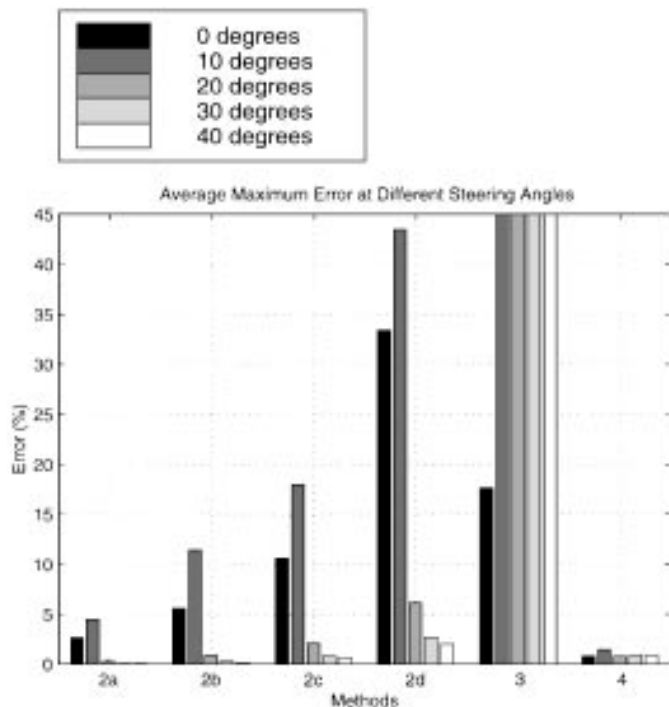

Fig. 7. Bar plots of average maximum error at different steering angles for method 2, 3, and 4. The errors of method 3 at steering angles larger than 10° are outside the range of the plot.
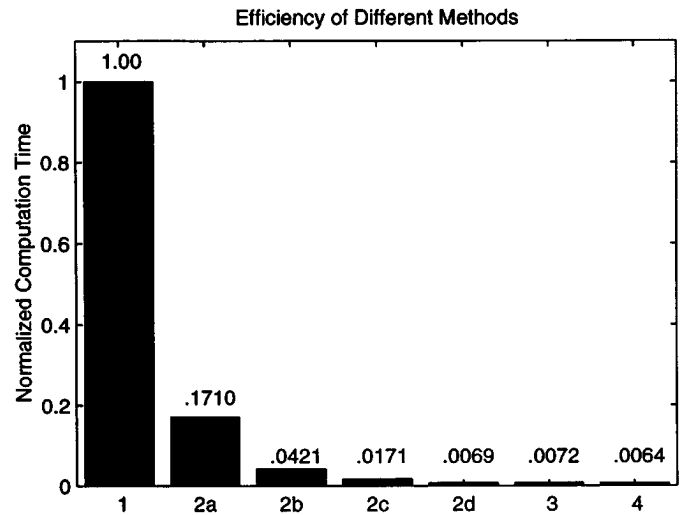

Fig. 8. Comparisons of computation time for all four beam simulation methods; the time is normalized by the time for method 1. Method 2a, 2b, 2c, and 2d uses sampling rates of 1.024 GHz, 512 MHz, 256 MHz, and 128 MHz, respectively. Method 3 is the Fresnel approximation, and method 4 is the frequency-domain model described here.

domain method increased by more than a factor of 4 when the sampling rate was increased from 512 MHz to 1.024 GHz, which suggests that cache performance started to degrade for this data size.

Results shown in Figs. 4 to 8 demonstrate that the frequency-domain model described in this paper performs very well in terms of accuracy, error spread, and computational efficiency.

IV. Simulation Results

The model is implemented in C/C++ on an Alpha/OSF platform using a DEC (Compaq, Houston, TX) compiler. The program makes use of standard library functions only; therefore, it can be ported to any other platform that supports C/C++. We trade memory usage for speed whenever possible because most machines today have a physical memory size of 64 MB or more.

To demonstrate the versatility of the model, we will present images of simulated point spread functions with different lateral focusing schemes, and images of objects containing "focal lesions".

A. Point Spread Functions

Point spread functions for different focusing schemes were generated by simulating images of isolated point targets using a 150 element linear array. Each element was modeled with dimensions of 10 mm × 150 μm, with 200 μm spacing between centers of adjacent elements. The pulse implemented is a 3.5 MHz Gaussian modulated sine wave with a 6 dB bandwidth of 50%. Because we are interested in lateral focusing effects, no elevational focusing was applied.
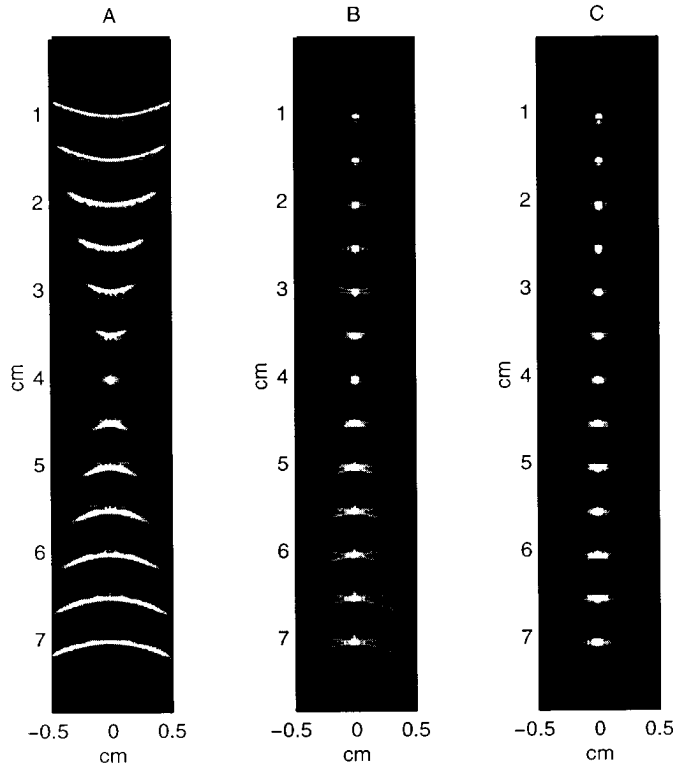
Fig. 9. Images of point spread functions at various depths, generated by the frequency domain model: (a) single transmit and receive focal distance of 4 cm; (b) a fixed transmit focus of 4 cm and a continuous receive focus and a dynamic aperture with a constant F/2 in the near field; (c) multiple transmit focal depths, dynamic F/2 aperture, and continuous receive focusing.
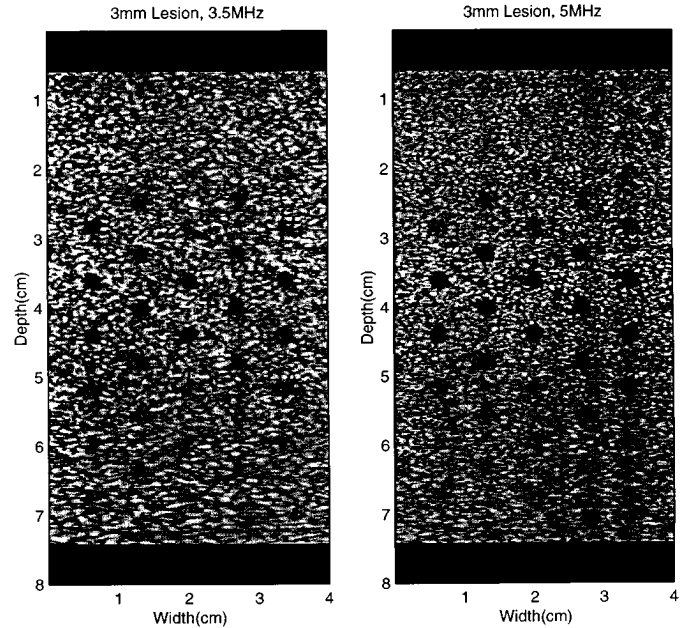

Fig. 10. Simulated images of a "3 mm spherical lesion" phantom, shown for a 3.5 MHz (left) and 5 MHz (right) center frequency pulse. The elevational focus is assumed to be 4 cm. Spherical lesions are positioned throughout the imaging plane.

The images in Fig. 9 illustrate the effects of several lateral focusing methods. The point spread functions are displayed over a 45 dB dynamic range. The different panels show the effects of using a single fixed transmit and receive focus at 4 cm [Fig. 9(a)]; single fixed transmit focus at 4 cm, and a continuous receiving focus, with a fixed receiving F/2 in the near field [Fig. 9(b)]; multiple transmit focal depths at 1, 2.5, 4, 5.5, and 7 cm with a constant F/2 in the near field, and continuous receiving focus with F/2 in the near field [Fig. 9(c)].

From the point spread function result, as expected, dynamic receiving focusing with dynamic aperture greatly improves the spatial resolution in the near and far field. In Figs. 9(b) and 9(c), we see the resolution degrades at large depths when the finite sized aperture results in the inability to maintain F/2.

B. Images of Lesion Phantoms

As a second example, we simulated images from a solid tissue-like phantom containing small spherical "lesions". The phantom material is assumed to have an attenuation coefficient of 0.5 dB/cm/MHz and a speed of sound of 1540 m/s. A 3 mm diameter spherical, low scatter objects are assumed to be positioned throughout the scan plane. The active aperture for each beam line is assumed to consist of 128 elements of size 150 μm $\times$ 10 mm, with a center-to-center distance of 200 μm. The lesion phantom is simulated by randomly distributed scatterers. The phantom simulated has a dimension of 4.5 cm $\times$ 2 cm $\times$ 7 cm; the scatterer number density is assumed to be 4000/cm^3. With our implementation, such a simulation took about 16.5 hours on a 500 MHz Alpha 21164 workstation

In this example, elevational focusing was applied; the elevational focus and the transmit focus both assumed to be 4 cm. The receive focus is continuous, and a dynamic aperture maintains a constant F/2 until reaching a limit due to aperture size. A Gaussian-shaped input pulse with a central frequency of either 3.5 MHz or 5 MHz was used; the 6 dB bandwidth was assumed to be 50%. Time gain control (TGC) was applied to compensate for attenuation.

Results of the simulation are presented in Fig. 10 for both the 3.5 MHz and the 5 MHz central frequency. The images illustrate the limited resolution brought about by slice thickness of current linear array transducers. Directly at the elevational focus, the 3 mm objects are visualized. However, they are not seen in the near field or in the far field. This type of behavior has been observed in experimental results using spherical lesion phantoms [15].

V. Discussion

Image simulation models can be effective tools for investigating how image quality depends on array transducer design and implementation. Displayed point spread function images, such as those in Fig. 9 allow evaluation of beam patterns for specific transducer parameters, such as the focal configuration, aperture function and apodization. Simulations of gray scale images also can provide

vivid demonstration of the effectiveness of both transducer and imaging parameters for detecting lesions of a given backscatter contrast and size. Although we did not attempt to match the transducer geometry and beam formation for any particular scanner in this study, the resolution pattern demonstrated in Fig. 10 is typical of those seen for clinical scanners imaging spherical lesion phantoms [15]. Future research will be directed toward more closely modeling specific transducer pulser-receiver systems to evaluate their effectiveness for detecting low contrast objects.

A variety of models for computing beam patterns and generating simulated images from array transducers have been described in the literature. The frequency domain simulation model described in this paper can be considered a suitable alternative to well-sampled time-domain impulse response methods, especially when computation time is an important factor. Although lower sampling rates of the impulse response also can shorten computation times, the frequency-domain model using the field approximation in (4) appears to be at least as effective in terms of accuracy, error spread, and efficiency.

Many physical features related to ultrasound imaging are frequency dependent, i.e., attenuation and backscattering. These properties appear in the frequency-domain formulation simply as multiplying factors, so it is trivial to incorporate them into the frequency domain model. In the time domain, various layers of convolution have to be added to model these frequency-dependent features. In addition, dispersion is more easily modeled in the frequency domain models. Yet another advantage of the method described in this paper is that (8) takes care of elevational focusing almost free of computational cost. To model elevational focusing in the time domain, one has to divide the element into smaller rectangles along the elevational direction, and this will substantially increase the computational cost and the error uncertainty.

To achieve acceptable accuracy in the simulation of real problems involving array transducers, the frequency-domain model described in this paper appears to be more efficient and flexible than sparse sampling applied to impulse-response models (method 2) or the Fresnel approximation (method 3). Compared to the "accurate" impulse response model, this frequency-domain model can reduce computation time by a factor of 150; the normal error is less than 1%, except in regions very close to the transducer. In addition, integration parameters can be readily changed to accommodate any accuracy required because the error in this method is more predictable than the other approximation schemes described here, as it only depends on the distance and has a very narrow spread.

VI. Conclusion

The frequency-domain simulation model described in this paper is computationally efficient and demonstrates very good accuracy and very small error spread for all steering angles. Realistic B-mode images can be obtained using this model. Many frequency-dependent imaging parameters and properties are more easily modeled in the frequency domain than in the time domain. Comparisons of different simulation methods show that the frequency domain approach is a valid and feasible method to model array transducers.

References

[1] G. Thupholme, "Generation of acoustic pulse by baffled plane pistons," *Mathematika*, vol. 16, pp. 209–224, 1969.

[2] P. Stephanishen, "Transient radiation from pistons in an infinite planar baffle," *J. Acoust. Soc. Amer.*, vol. 49, pp. 1629–1638, 1971.

[3] J. Emeterio and L. Ullate, "Diffraction impulse response of rectangular transducers," *J. Acoust. Soc. Amer.*, vol. 92, pp. 651–662, 1992.

[4] J. Jensen, "Ultrasound fields from triangular apertures," *J. Acoust. Soc. Amer*, vol. 100, pp. 2049–2056, 1996.

[5] M. Arditi, F. Foster, and J. Hunt, "Transient fields of concave annular arrays," *Ultrason. Imaging*, vol. 3, pp. 37–61, 1981.

[6] P. Crombie, A. Bascom, and S. Cobbold, "Calculating the pulsed response of linear arrays: Accuracy vs. computational efficiency," *IEEE Trans. Ultrason., Ferroelect., Freq. Contr.*, vol. 44, pp. 997–1009, 1997.

[7] J. Goodman, *Introduction to Fourier Optics*. New York: McGraw-Hill, 1968, pp. 57–61.

[8] J. Jensen and N. Svendsen, "Calculation of pressure fields from arbitrarily shaped, apodized and excited ultrasound transducers," *IEEE Trans. Ultrason., Ferroelect., Freq. Contr.*, vol. 39, pp. 262–267, 1992.

[9] J. Jensen and P. Munk, "Computer phantoms for simulating ultrasound B-mode and CFM images," in *Proc. 23rd Acoust. Imaging Symp.*, 1997, pp. 75–80.

[10] D. Turnbull and F. Foster, "Beam steering with pulsed two-dimensional transducer arrays," *IEEE Trans. Ultrason., Ferroelect., Freq. Contr.*, vol. 38, pp. 320–333, 1991.

[11] J.-Y. Lu and J. Greenleaf, "A study of two-dimensional array transducers for limited diffraction beams," *IEEE Trans. Ultrason., Ferroelect., Freq. Contr.*, vol. 41, pp. 821–827, 1994.

[12] W. Press, S. Teukolsky, W. Vetterling, and B. Flannery, *Numerical Recipes in C*. Cambridge, MA: Cambridge Univ. Press, 1992, pp. 255–259.

[13] P. Morse and K. Ingard, *Theoretical Acoustics*. Princeton, NJ: Princeton Univ. Press, 1986, Chapters 7–8, pp. 306–441.

[14] M. Insana and D. Brown, "Acoustic scattering theory applied to soft biological tissues," in *Ultrasound Scattering in Biological Tissues*, K. Schung and G. Thieme, eds. Boca Raton, FL: CRC Press, 1993, Chapter 4, pp. 75–124.

[15] J. Rownd, E. Madsen, J. Zagzebski, G. Frank, and F. Dong, "Phantoms and automated system for testing resolution of ultrasound scanners," *Ultrason. Med. Biol.*, vol. 23, pp. 245–260, 1997.

Yadong Li received his B.S. in electrical engineering from Beijing University, China, in 1995. Currently, he is pursuing the Ph.D. degree in physics and a M.S. degree in computer science at the University of Wisconsin-Madison.

His research interests include ultrasound imaging, B-mode image texture analysis, and computer modeling in ultrasound.

James A. Zagzebski (A'89) was born in Stevens Point, WI, in 1944. He received the B.S. degree in physics from St. Mary's College, Winona, MN, and the M.S. degree in physics and the Ph.D. degree in radiological sciences from the University of Wisconsin, Madison. He is Professor of medical physics and of radiology and human oncology at the University of Wisconsin.

His research interests include ultrasound imaging and tissue characterization, flow detection and visualization using ultrasound, and technological assessment of imaging devices.

Dr. Zagzebski's professional affiliations include the IEEE, the American College of Radiology, the American Institute of Ultrasound in Medicine, and the American Association of Physicists in Medicine.